Acta Materialia 183 (2020) 274–284

Contents lists available at ScienceDirect

Acta Materialia

journal homepage: www.elsevier.com/locate/actamat

Full length article

On the mechanical heterogeneity in dual phase steel grades: Activation of slip systems and deformation of martensite in DP800

Chunhua Tian, Dirk Ponge, Leon Christiansen, Christoph Kirchlechner*

Max-Planck-Institut für Eisenforschung GmbH, D-40237 Düsseldorf, Germany

ARTICLE INFO

Article history:
Received 24 May 2019
Revised 10 October 2019
Accepted 1 November 2019
Available online 12 November 2019

Keywords:
DP steel
Ferrite
Martensite
Dislocation
Void nucleation
Slip system
Failure, {123} slip

ABSTRACT

We used micropillar compression experiments to study the plasticity of ferrite and martensite of two commercial dual phase steel grades (DP800). The activation of all three slip plane families, namely {110}, {112}, {123}, was observed in single crystalline ferrite pillars. They exhibit a comparable mean critical resolved shear stress (CRSS) of 147 ± 6, 143 ± 9, 146 ± 4 MPa for 3 μm pillars and are predominantly following Schmidś law. A distinct size effect occurs when comparing the CRSS of 2 μm and 3 μm pillars. Martensite islands show uniform deformation and exhibit high compressive yield strength up to nearly 3 GPa. In most cases martensite pillars deform in an isotropic fashion without distinct slip traces. Despite the identical ultimate tensile stress of two steel grades their ferrite CRSS and martensite strength are largely different. It is found that the softer ferrite results in a lower macroscopic yield strength and a higher elongation to failure during macroscopic tensile testing. The results suggest that an increased local strain hardening capability suppresses global damage. The data provided here can serve as input parameter for crystal plasticity modeling.

1. Introduction

Dual phase (DP) steels – comprised of a soft ferrite matrix and dispersed hard martensite islands – are widely used as structural material, e.g., for automotive applications because they offer a good combination of high strength and ductility. Furthermore, strength and ductility can be controlled by several metallurgical and thermomechanical factors including the carbon content, additional alloying elements, or heat treatments to tune the martensite volume fraction, the grain size of ferrite and martensite as well as the texture [1–5]. Because of their special composite structure, DP steels behave heterogeneously during deformation at the microstructural length scale. Also, the heterogeneity complicates the understanding of the deformation behavior, particularly during damage initiation and growth, which has been intensively investigated both by experiments and modeling work. Experimentally, the heterogeneity is characterized either through analyzing the strain localization and the evolution of damage [6–8] by digital image correlation (DIC) in situ or by the electron backscatter diffraction (EBSD) based kernel average misorientation (KAM) [9]. In case of modeling a representative volume element (RVE) based on the real microstructure is used to analyze stress and strain partitioning upon loading [10,11].

While the important role of heterogeneity on the mechanical behavior of DP800 is evident, an explicitly quantitative and mechanism based description of the mechanical properties of ferrite and martensite and their impact on damage initiation and growth had rarely been studied. Srivastava et al.' [12–14] significantly contributed to this field by measuring the compressive yield strength of individual phases via pillar compression. Also, they calibrated a crystal plasticity finite element model (CP-FEM) using their experimental stress–strain curves of ferrite pillars [12,14,15]. However, a comprehensive study on the activation of different slip systems and a thorough analysis of the critical resolved shear stress of single crystalline ferrite is still lacking. This data can then serve as input parameter in CP-FEM, for which constitutive models of deformation at the single grain level are vital. The most prominent parameter of these models is the CRSS of all contributing slip systems. Despite the controversy on activated slip systems in body centered cubic (bcc) iron it became common practice to assume {110}⟨111⟩ and {112}⟨111⟩ slip systems only [16–18]. This practice partially ignores the experimental observations of slip on the other closed packed planes, like {123}. Due to the lower velocity compared to edge dislocation, screw dislocation motion is controlling

* Corresponding author.
E-mail address: kirchlechner@mpie.de (C. Kirchlechner).

https://doi.org/10.1016/j.actamat.2019.11.002

Table 1
Chemical composition in weight percent (%) as determined by wet-chemical analysis for both DP800 steel grades denoted DP1 and DP2.

	C	Si	Mn	P	S	Al
DP1	0.131	0.206	1.51	0.008	0.0023	0.03
DP2	0.131	0.194	1.69	0.0088	0.0016	0.038
	Cr	Mo	Nb	Ti	V	B
DP1	0.0187	< 0.005	0.0188	0.0014	0.0084	< 0.001
DP2	0.718	0.0035	< 0.001	0.0303	0.0027	< 0.001

the plastic deformation of bcc [19]. The core structure of screw dislocation in bcc is non-planar, which is commonly regarded as the key reason for the breakdown of Schmidś law in bcc materials [20]. Gröger and Vitek [21] proposed that not only the resolved shear stress on the slip plane in the slip direction but also the entire stress state play an important role for CRSS. All these factors result in a complex, time, temperature and orientation dependent dislocation slip behavior, which requires constitutive material laws for simulating bcc materials by CP-FEM.

Micropillar compression [14] is the ideal tool to study microstructure heterogeneity at the micron level as it can be used to isolate individual phases, grains or interfaces and estimate the local CRSS by analyzing the activated slip system [22–24]. Within this study we are applying micropillar compression to measure the mechanical properties of bcc ferrite and martensite of two different DP800 steel grades with an identical macroscopic ultimate tensile strength (UTS) but different elongation to failure. We show that – in both cases – three different slip system families behave identically in terms of CRSS and that – in our case – the Schmid factor is the dominant cause for slip system activation. The results are also used to explore pathways for reducing the damage occurring during metal forming.

2. Experimental procedures

2.1. Microstructure characterization

We have investigated two types of DP800 steel that subsequently named DP1 and DP2. If not specifically mentioned, the presented results are obtained on DP2. Their chemical composition was analyzed by wet-chemical analysis (Table 1). The latter was additionally zinc-coated and the thickness of both steel sheets is 1.5 mm. Before conducting any microstructural characterization or focused ion beam (FIB) milling, the specimens were first cut into pieces of 8 × 5 × 1.5 mm, ground and polished by a 30 nm oxide polishing suspension (OPS). Electron Channeling Contrast Imaging (ECCI) was performed to investigate the dislocation structure in ferrite using a Zeiss Merlin® field emission microscope operated at 30 kV. Besides, EBSD was conducted to investigate the grain size distribution of ferrite and martensite, as well as the substructures formed in martensite islands. Discrimination of ferrite and martensite was based on the EBSD confidence index (CI) of the two phases. The volume fraction of individual phases was measured using point counting. For this, the OPS polished samples were etched in 1% Nital solution for 5 s and investigated via scanning electron microscope (SEM).

2.2. Element characterization by atom probe tomography

Atom probe tomography (APT) was conducted to measure the local distribution of chemical elements, particularly C. The needle-like APT tips were prepared by FIB milling (FEI Helios NanoLab 600TM). A final cleaning step using 5 kV and a current of 15 pA was applied to minimize Ga ion damage on the tip surface. The APT experiments were conducted on a CAMECA instrument LEAP™ 5000 XR (reflection-fitted with a flight path 382 mm) using the voltage mode. The base temperature was set to be 60 K. The detection rate is 0.5%, pulse fraction 20% and pulse rate 250 kHz. The data analysis to reconstruct the 3D atom map was done using the software package IVAS®.

2.3. Mechanical testing

Both, macro and micro mechanical tests were performed. Micro compression experiments were carried out to determine the CRSS, activated slip systems of ferrite and the strength of martensite. We applied a Zeiss Auriga® Dual beam FIB on the OPS polished sample surface to mill annular pillars with a diameter of 1–3 µm for ferrite. Due to the small colony size, the martensite pillars were limited to a maximum diameter of 800 nm. The aspect ratio (height/diameter) is ranging from 2 to 4. A three-step milling strategy using 30 keV Ga^+ ions was used: rough milling of an outer ring with 16 nA ion current, a middle ring 2 nA and fine milling with 240 pA.

Subsequently, on top of the ferrite pillars, EBSD was performed at 15 kV using the same Zeiss Auriga® microscope equipped with an EDAX system with Hikari® charged coupled device (CCD) and the TSL OIM 7 software package in order to measure the crystallographic orientation of the single crystalline ferrite pillar.

After the sample preparation, in situ micropillar compression tests were conducted using an Asmec Unat II (Asmec GmbH, Radeberg, Germany) in displacement mode. The indenter was equipped with a flat diamond tip provided by Synthon MDP (Switzerland). A loading rate of 1×10^{-3} s^{-1} was applied. During deformation, the pillars were imaged in a Zeiss Gemini500 field emission microscope using the secondary electron (SE) and InLense® detectors. For the calculation of the engineering stress versus engineering strain curves, the force was divided by the top diameter and displacement by the initial pillar height.

After the *in situ* test, the compressed pillars were imaged using the abovementioned microscopes. Based on the orientation information obtained by the top surface EBSD scans and the imaging conditions prior to deformation, we superimposed all 48 possible slip systems on the pillar surface. For an accurate identification of the {110}, {112} and {123} slip systems, we considered the non-zero taper angle of the pillars and compared the experimental slip pattern with the superimposed predictions. Accordingly, the CRSS can be calculated by taking the engineering normal stress σ and the Schmid factor m of the activated slip system into account and applying $\tau = \sigma.m$. Please note that throughout the manuscript the term slip plane corresponds to the effective slip plane and not – as pointed out later – to the atomistic plane of slip.

3. Results and interpretation

3.1. Characterization and tensile result

We have performed microstructure characterization and analyzed the element distribution of two commercial DP steels. The microstructures of both DP steel grades exhibit a banded morphology of martensite and partly dispersed martensite islands in the ferrite matrix (see labeled banded martensite with double ended arrow in Fig. 1a and b). The martensite volume fraction of DP1 and DP2 was evaluated by point counting in 10 regions, which is comparable for both steel grades 42 ± 1% and 38 ± 1%.[1] However, the grain size distribution shows larger martensite colonies

[1] Unless otherwise stated the error bars are always provided as the error of the mean.

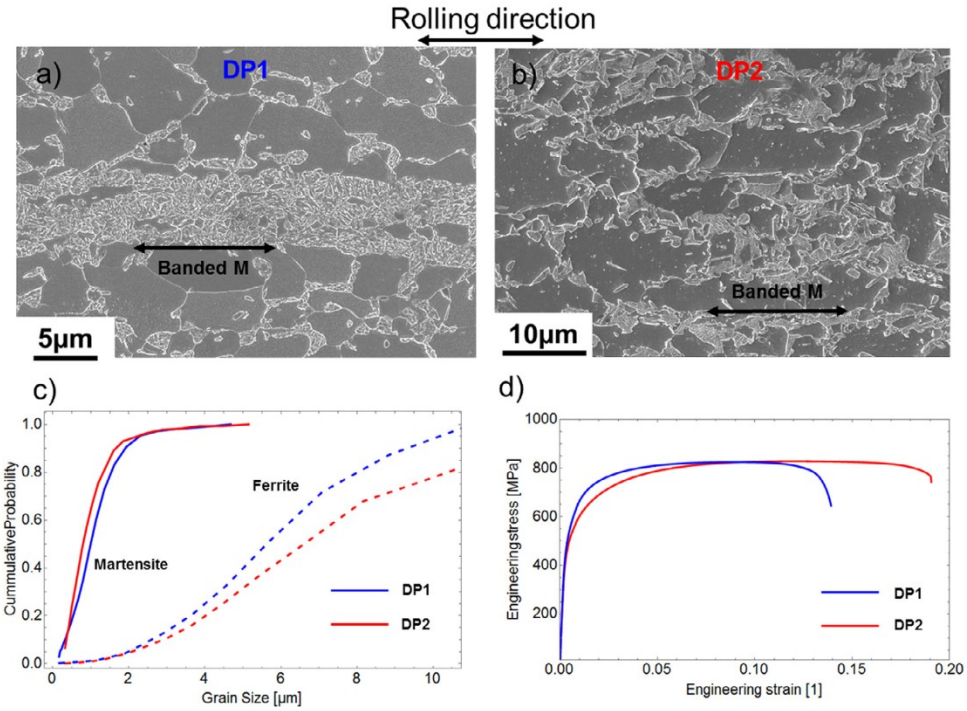

Fig. 1. Secondary electron image of (a) DP1 and (b) DP2 steels. (c) Grain size distribution of ferrite and colony size of martensite for both steel grades. (d) The macroscopic tensile test results for both steel grades.

and smaller ferrite grains in DP1 compared to DP2 (Fig. 1c). The average colony size of martensite is 1.1 ± 0.1 μm and 1.0 ± 0.1 μm, while of ferrite grains it is 5.9 ± 0.1 μm and 7.0 ± 0.1 μm, correspondingly.

The engineering stress versus strain curves obtained by the macroscopic tensile testing (Fig. 1d, according to DIN EN ISO 6892-1) shows two distinct differences of the two steel grades in rolling direction: (i) DP1 yields at 530 MPa which is 36 MPa higher compared to DP2 (494 MPa). (ii) Also, DP1 fractures at an elongation of 14.4% which is lower compared to DP2 with a strain to failure of 18.6%. Similarly, the uniform elongation of DP1 is also smaller (compare 8.8% and 11.5%). Nevertheless, both steel grades reach an identical ultimate tensile strength of 830 MPa.

The martensite colonies have a complex substructures as shown in Fig. 2a and b. They exhibit a hierarchical structure with lath morphology. The laths reveal a well-known orientation relationship to the parent austenite, namely, $\{111\}_\gamma$ // $\{110\}_\alpha$ and $\langle 110\rangle_\gamma$ // $\langle 111\rangle_\alpha$ being consistent with literature (e.g., [25]). The packets are highlighted in Fig. 2a and b by white lines and the variants are labeled by numbers. Within our islands we do not simultaneously see all 24 variants expected for one prior austenite grain. Even in one packet, the variants are not complete as we observe less than 6 variants (see for instance the packet 1 in Fig. 2a). The block width of martensite in both DP grades is similar and of the order of 100 nm (see black arrow Fig. 2a and b). However, the martensite islands in DP1 contain more prior austenite grain boundaries.

In addition, we have applied ECCI to investigate the dislocation structure in selected ferrite grains (Fig. 2c and d). Both DP grades have a high dislocation density in ferrite which is approximately $4.5\cdot10^{13}$ m^{-2} for DP1 and $1.6\cdot10^{13}$ m^{-2} for DP2. Besides, a dislocation density gradient exists with low dislocation density in the ferrite interior towards a higher dislocation density near the phase boundary (see Fig. 2c and d, along the arrow).

We further measured the local element distribution using APT to thoroughly understand the differences of both dual phase steels. One example is presented in Fig. 3, showing the elemental distribution at a ferrite/martensite boundary from DP2. Two aspects are observed: First, there is an enrichment of Mn, Cr and C along the interphase boundary but a homogenous distribution of Mn and Cr in ferrite and martensite. Second, almost all carbon is located inside the martensite, where the C content reaches an average value of 3.12 ± 0.13 at.%. The result is consistent with three other pure martensite tips from the same DP grade. However, the C content drops significantly to 0.28 ± 0.03 at.% inside ferrite. The content of Mn, Cr and Si in martensite are 2.08 ± 0.05 at.%, 0.80 ± 0.04 at.% and 0.58 ± 0.03 at.% while in ferrite they reach 1.37 ± 0.03 at.%, 0.52 ± 0.03 at.% and 0.44 ± 0.02 at.%. Note that the element distribution is consistent within three pure ferrite and martensite tips of DP2. DP1 has a similar chemical composition of ferrite except that it contains almost no Cr (0.03 ± 0.01 at.%), which is consistent with the wet chemical analysis (Table 1).

Differences of the carbon distribution inside the martensite of the two DP steel grades are shown in Fig. 4, where the 5 at.% carbon isosurface is used. The C distribution is heterogeneous in martensite, especially in DP1 where it locally can reach up to 25 at.% (Fig. 4c), implying that Fe_3C carbides formed in the martensite in DP1. The forming sites are very likely to be at block boundaries, since the two highly carbon concentrated isosurfaces have a distance of the order of 100 nm which correlates well with the block width (see Fig. 2a). By contrast, the carbon enrichment in martensite in DP2 is significantly lower (maximum up to 10 at.%) and the distance between regions with high C content is smaller. Hence, here we conclude that C is enriched either at laths boundaries or at dislocation lines, but not at block boundaries.

3.2. Micro plasticity of ferrite

This chapter mainly describes the DP2 steel grade. For determination of the activated slip system and the CRSS we combine *post mortem* SEM images and snapshots taken from the in situ deformation. By this approach we can identify the slip system activated first which will be the one analyzed subsequently. Differences between the two steel grades DP1 and DP2 are summarized in the last Section 3.2.4 of this chapter.

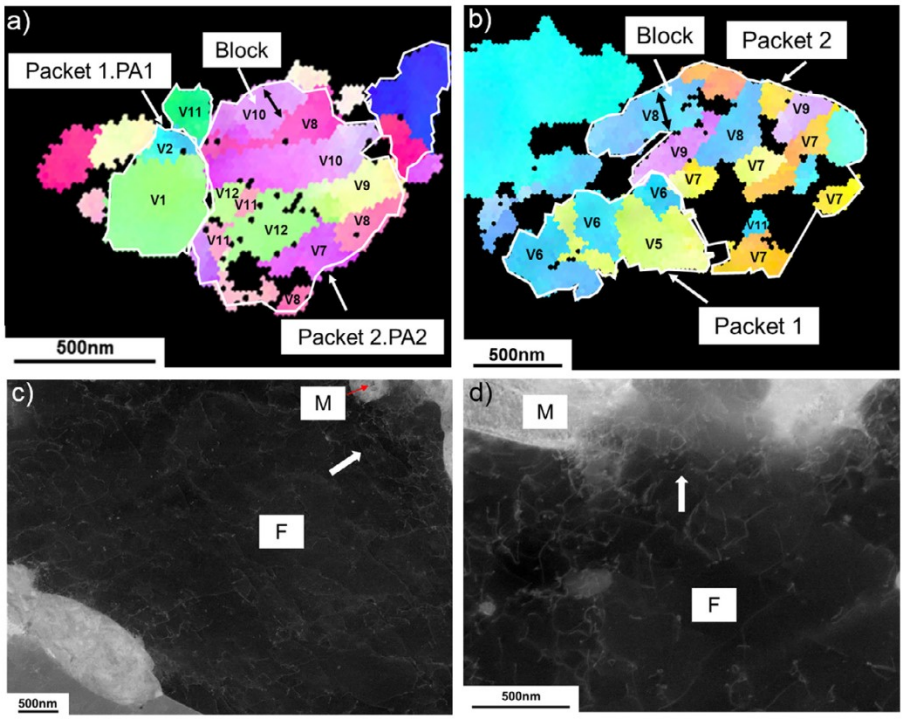

Fig. 2. (a) and (b) are the IPFs of two martensite islands out of DP1 and DP2, respectively, showing the identified substructures. Detailed interpretation of variants is referred to [25]. (c) and (d) are the ECCI images of DP1 and DP2. F represents ferrite and M means martensite.

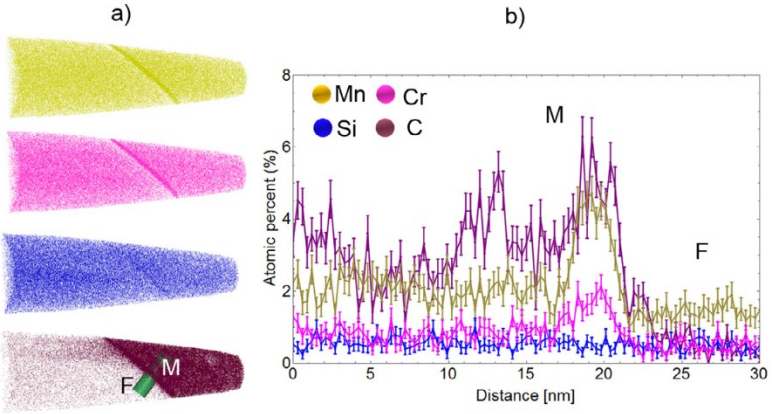

Fig. 3. (a) One representative APT tip from DP2 with ferrite and martensite phase boundary showing elements distribution; (b) element content variation along the green cylinder region. (For interpretation of the references to color in this figure legend, the reader is referred to the web version of this article.)

3.2.1. Measuring the cumulative distribution function (CDF) of the CRSS

Micro compression testing was performed to analyze the CRSS in the ferrite grains with different orientations. The crystallographic slip plane was indexed on in situ and *post mortem* SEM images using EBSD data as described above. The code thereby is superimposing the {110}, {112} and {123} plane families as typically observed for bcc structures (Fig. 5, Column III).

In far most cases, the single crystalline compression pillars exhibited only one dominating slip plane after an engineering strain between 10% and 15% (see for instance Fig. 5a). All three slip plane families are found active during pillar compression in our tested samples with examples for every family presented in each row of Fig. 5. In total, eight successfully tested pillars activate the {110} slip planes, six pillars the {112} and twelve pillars the {123} first. The corresponding activated slip system and Schmid factor are given in Table 2. As expected from Schmidś law all activated slip systems have a very high Schmid factor, however, not necessarily the highest (e.g., Ferrite C), especially if several slip systems exhibit a similar value. This phenomenon has been reported previously by Ng and Ngan [26] and is rather attributed to the limited number of dislocation sources in the finite pillar volumes than to non-Schmid

Table 2
Analysis of the activated slip systems for pillars presented in Fig. 5. The three closest planes possibly matching the experimental pattern best are shown. The identified slip system and corresponding Schmid factor are highlighted.

Representative pillars	Drawn slip systems	Schmid factor	Compressive yield strength /[MPa]	CRSS /[MPa]
Ferrite A	$(0\bar{1}1)[\bar{1}11]$	**0.50**	277	138
	$(13\bar{2})[\bar{1}11]$	0.48		
	$(1\bar{2}3)[\bar{1}11]$	0.46		
Ferrite B	$(\bar{1}12)[1\bar{1}1]$	**0.50**	334	166
	$(\bar{2}13)[1\bar{1}1]$	0.49		
	$(\bar{1}23)[1\bar{1}1]$	0.49		
Ferrite C	$(0\bar{1}1)[\bar{1}11]$	0.49		
	$(13\bar{2})[\bar{1}11]$	**0.49**	304	149
	$(12\bar{1})[\bar{1}11]$	0.46		

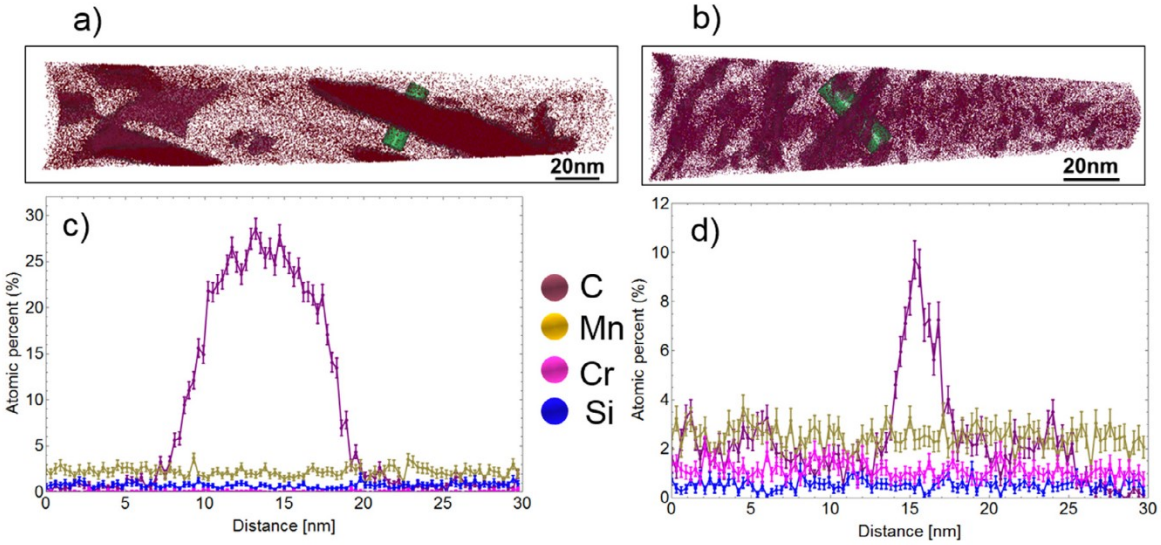

Fig. 4. (a) and (b) show the carbon distribution in two martensite tips from DP1 and DP2 together with the 5 at.% carbon isosurface. (c) and (d) are element content variation inside the two green cylinder regions. The two cylinders have the same size. (For interpretation of the references to color in this figure legend, the reader is referred to the web version of this article.)

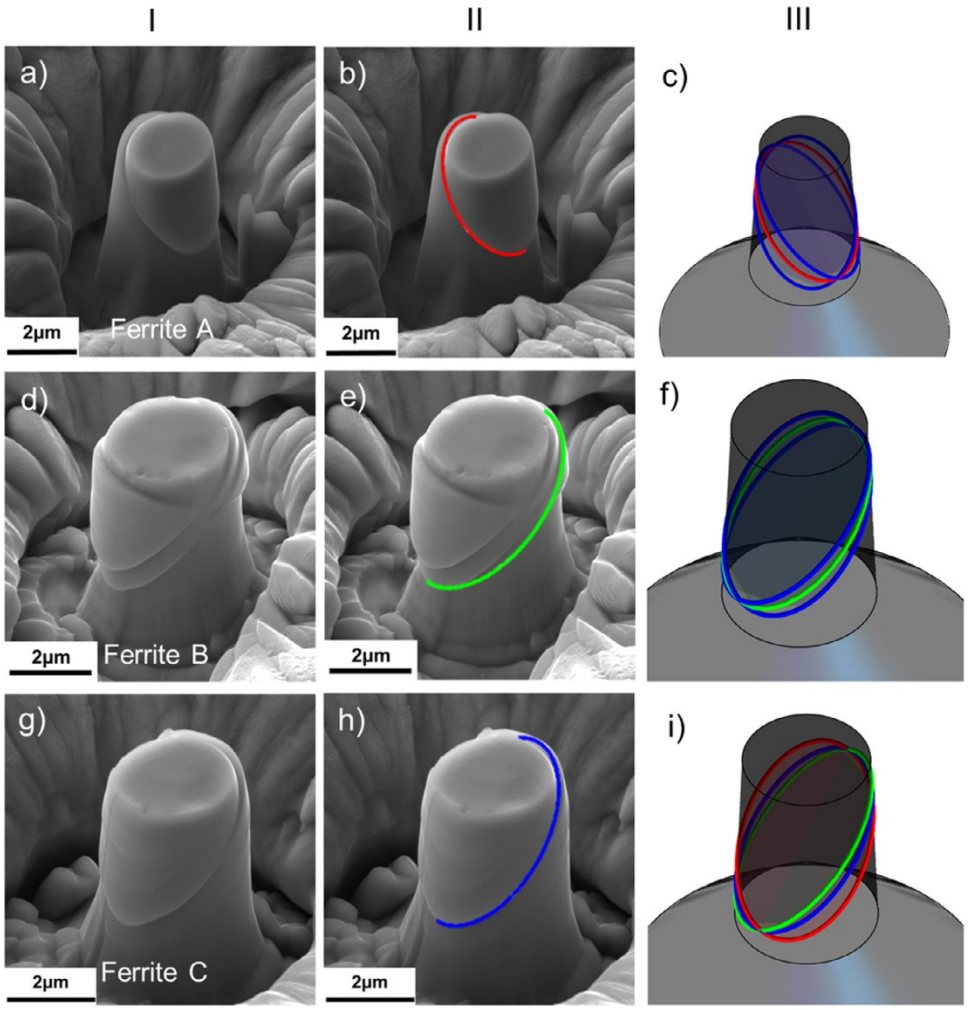

Fig. 5. Slip traces in ferrite. Column I presents the post mortem SEM images. Column II shows superimposed identified slip traces and column III additional but not identified slip traces. Pillar (a), (d) and (g) are representative for {110}, {112} and {123} slip plane activation, respectively.

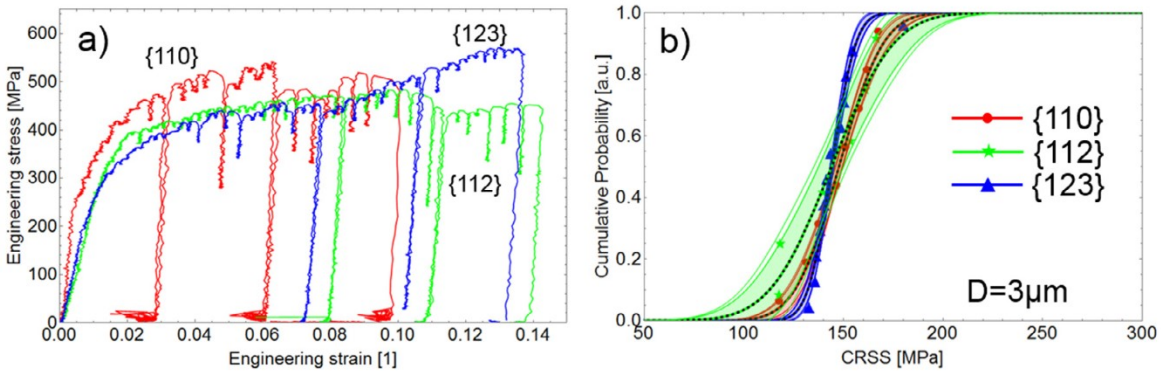

Fig. 6. (a) Engineering stress versus strain curves for three representative pillars, labeled with the determined activated slip plane. (b) The cumulative probability function (CPF) of the CRSS for the three slip plane families. In total, twenty-six 3 μm sized samples of the DP2 steel grade are used for this plot.

Table 3
Summary of the CRSS of ferrite pillars of the two steel grades and different diameters. The mean CRSS value and the dispersion of the CRSS are given. In both cases the error bars are given as the standard error of the mean.

Steel grade	Pillar size	Slip planes	Mean value [MPa]	Dispersion width [MPa]
DP1	2 μm	{110}	239 ± 16	32 ± 5
		{112}	197 ± 16	46 ± 7
		{123}	220 ± 17	41 ± 12
	3 μm	{110}	205 ± 8	25 ± 6
		{112}	204 ± 6	11 ± 5
		{123}	199 ± 9	29 ± 3
DP2	2 μm	{110}	179 ± 11	38 ± 2
		{112}	185 ± 12	30 ± 10
		{123}	172 ± 7	11 ± 3
	3 μm	{110}	147 ± 6	17 ± 1
		{112}	143 ± 9	24 ± 4
		{123}	146 ± 4	9 ± 1

effects. When a second slip system is activated (e.g., shown in Ferrite B), only the first activated system as determined by the in situ recording was taken for the subsequent CRSS calculation.

The engineering stress versus engineering strain curves of the single crystalline micro pillars show a jerky-like flow typical for the investigated size regime (see Fig. 6a) [24,27,28]. The engineering stress at a plastic strain of 0.5% was taken to compute the CRSS based on the previously identified slip plane.

Finally, the cumulative distribution function (CDF) of the CRSS was plotted for all three slip plane families (see. Fig. 6b) and fit by a Gaussian distribution as summarized in Table 3. In case of 3 μm sized pillars the mean CRSS of the {110} family equals 147 ± 6 MPa, of the {112} 143 ± 9 MPa and of the {123} 146 ± 4 MPa. Hence, surprisingly, within the standard error of the mean value, the CRSS of all three families is identical (here shown for 3 μm sized pillars of the DP2 steel grade).

3.2.2. Size effects of the DP2 steel grade

Ferrite grains exhibit a clear size effect (see Fig. 7 for the {110} 111 slip system) with 2 μm sized pillars being systematically stronger than their 3 μm sized counterparts (2 μm: 179 ± 11 MPa, 3 μm: 147 ± 6 MPa). Also, the 2 μm sized pillars show a higher dispersion, as evident from the distribution width in the cumulative distribution plot (see Fig. 7a) and the scatter in CRSS for pillar diameters (see Fig. 7b). Unfortunately, it is impossible to test pillars larger than 3 μm in diameter due to the limited grain size and smaller pillars than 1 μm due to the limited force resolution of the indenter, which prevents a meaningful quantification of a size scaling law.

3.2.3. Orientation effects on the activation of slip systems in the DP2 steel grade

The aforementioned CRSS distribution of the three families as well as their size distribution might also allow for analyzing orientation effects on the CRSS. For this purpose we have color coded the activation of the {110} ⟨111⟩, {112} ⟨111⟩ and {123} ⟨111⟩ slip systems in an inverse pole figure (IPF, see Fig. 8a). The plot thereby assumes an identical CRSS of all three slip system families, which agrees well with the findings reported in Section 3.2.1.

In addition, the experimentally identified slip systems for 2 and 3 μm sized pillars are presented in Fig. 8b and c. In case of the 3 μm sized pillars the experimentally observed slip system activation predominantly follows the Schmid predictions with only few outliers documenting the dominance of Schmidś law for the 3 μm sized samples. In case of 2 μm sized pillars the number of outliers seems to slightly increase (see Fig. 8e), nevertheless, the majority of pillars still follow Schmidś law and non-Schmid effects do not play a significant role in slip activation here. We address the outliers to the limited number of dislocation sources in the finite sample volume which results in a statistical "Break Down of Schmidś law" as proposed by Ng and Nghan [26]. Also, it should be noted that in the case of outliers the CRSS of the activated slip system is very close to the CRSS of the primary slip system exhibiting the highest available Schmid factor.

3.2.4. Grade effect of DP1 and DP2

Finally, let us focus on the differences of the ferrite of the two steel grades DP1 and DP2 as shown in Fig. 9. The 3 μm pillars milled from DP1 systematically yield at a significantly higher stress and exhibit a substantially higher CRSS as compared to the ones obtained from DP2. The mean CRSS of DP1 {110} slip plane group reaches 205 ± 8 MPa, which is approximately 60 MPa larger in comparison to147 ± 6 MPa of DP2 (see Fig. 9b and c).

Similar to the previously described size scaling in DP2 (see Section 3.2.2), the 2 μm pillars of DP1 show a very broad distribution of the CRSS ranging from 200 MPa to 300 MPa, while the 3 μm are less dispersed. Hence, comparing the two steel grades with macroscopically identical UTS we can conclude that, irrespective of the pillar size, DP1 exhibits a higher yield strength than DP2.

As a summary, the results of all the tested pillars are given in Table 3 with the mean value and dispersion width of CRSS. The abovementioned points in terms of activated slip planes, orientation dependence and size effect are valid as well in the DP1 steel grade.

3.3. Micro plasticity of martensite islands

Within this section we focus on the deformation behavior of the martensite islands with their complex colony structure. The

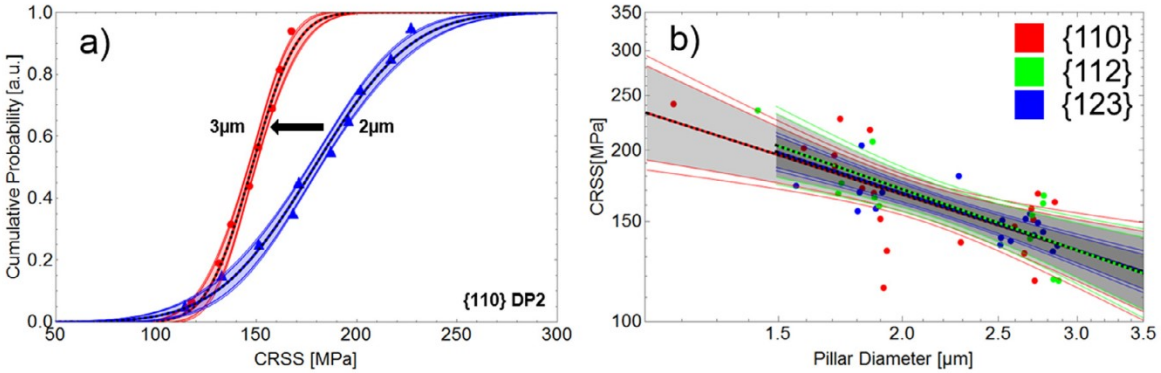

Fig. 7. (a) The CRSS distribution curves of 2 µm and 3 µm sized pillars of DP2. (b) Size scaling of the CRSS in the size regime from 1 µm to 3 µm.

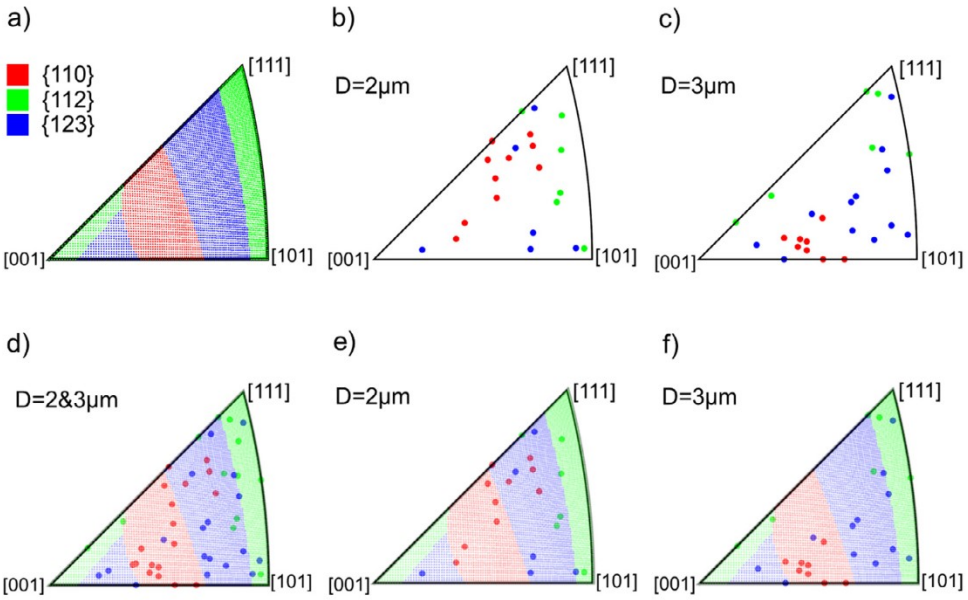

Fig. 8. (a) A colored IPF that shows the region where {110}, {112} or {123} plane groups possess the highest Schmid factor. (b) and (c) are the tested orientations of 2 µm and 3 µm ferrite pillars. They are colored according to experimentally identified activated primary slip planes, {110} as red, {112} as green and {123} as blue. (d)–(f) comparison of the experimental data points with the distribution of highest Schmid factor. (For interpretation of the references to color in this figure legend, the reader is referred to the web version of this article.)

hierarchical microstructure of our martensite islands, including a number of interfaces forming a complex substructure, is shown in the IPF (see Fig. 10a). The block size (see Fig. 10a) typically reaches dimensions of approximately 100 nm. Therefore, our micropillars do not contain one isolated martensite block but involve single martensite islands including their complex substructure.

During pillar compression, we observe barreling of the entire pillar which is occasionally accompanied by discrete slip traces. The discrete slip traces had previously been interpreted as slip at block-boundaries [29–31]. Also in our case the block size as measured from EBSD image quality (IQ, Fig. 10b) maps show a similar dimension as observed in the slip traces in Fig. 10e. Furthermore, as proven through the ⟨110⟩ pole figures of the substructures 1 and 2 (Fig. 10c), the interface between them is a block boundary. Hence, the discrete slip traces on the pillar surfaces are consistent with the interpretations of Du et al. [29] and Mine et al. [31].

Also the engineering stress versus engineering strain curves (see Fig. 11a) document the deformability of martensite islands at the micron scale. After linear elastic loading the martensite of both DP grades exhibit significant plastic deformation during the compression experiment. Even though some stress drops occur in the microscale martensite, the overall appearance of the engineering stress vs. strain curve is much smoother compared to the ferrite pillars.

Due to the limited martensite island size the martensite pillars might contain softer ferrite at the bottom, which significantly influences the stress strain behavior (see black curve in Fig. 11a). By testing more than 30 pillars, we differentiated such cases by two aspects: (i) the ferrite containing pillars tend to exhibit a sink-in upon compression, where the entire pillar or parts of it can be pushed into a plastically deforming ferrite island (see Fig. 10d); (ii) fully martensitic pillars exhibit significantly higher flow stresses among the compression engineering stress versus engineering strain curves (see Fig. 11a). Following this approach we cannot exclude the possibility of a significantly softer martensite at the bottom of our martensite pillars, similar as previously observed in TEM [14]. Therefore, our data only contains the high strength martensite and would not allow to discuss the occurrence of low strength martensite – if at all existing or present.

In this way, the pure martensite pillars of both DP steels and their strength distribution function were analyzed (see Fig. 11b). The martensite islands in both DP1 and DP2 yield at a surprisingly high mean stress level of 2716 ± 62 MPa and 2880 ± 49 MPa, respectively, i.e., on average, martensite colonies in DP1 have a slightly lower yield strength.

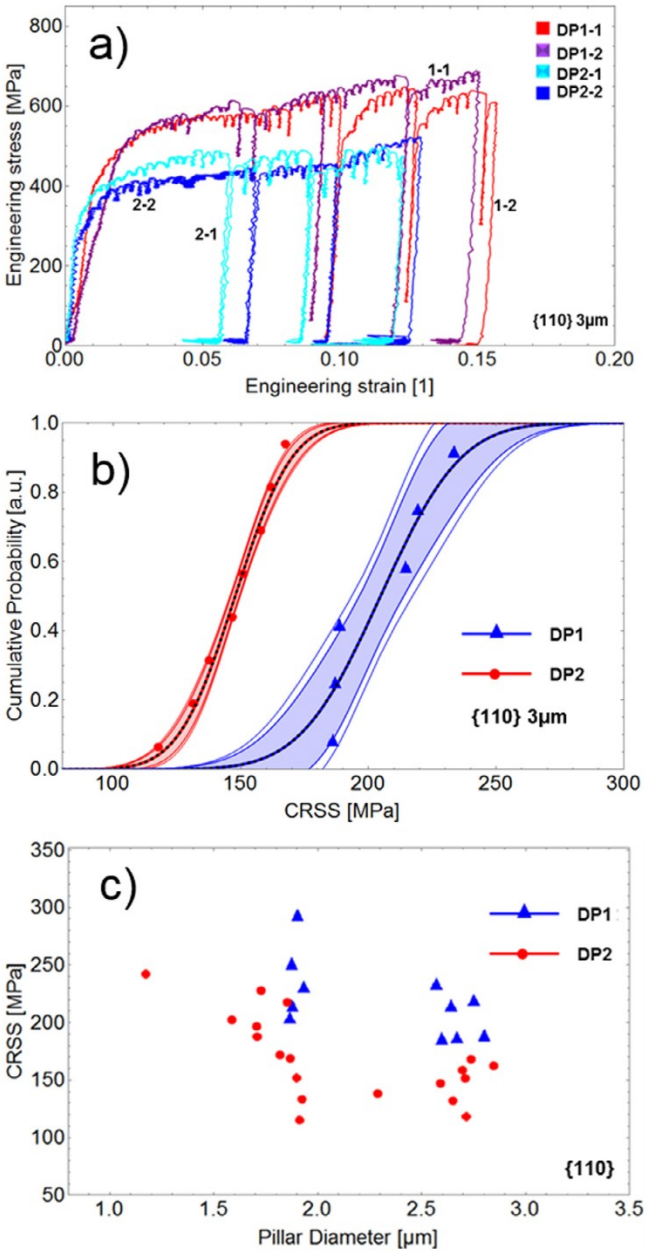

Fig. 9. Comparison of two DP800 steel grades: (a) Engineering stress versus strain curves of ferrite compression pillars; (b) the ferrite CRSS distribution of 3 µm pillars and (c) the size scaling plot of the CRSS in the limited size regime from 1 µm to 3 µm. Only {110} slip systems are shown.

4. Discussion

4.1. Slip systems of ferrite

We performed micropillar compression tests on the microstructure constituents ferrite and martensite in DP800 to microscopically investigate their deformation behavior to deeper understand their macroscopic mechanical behavior. Our BCC ferrite pillars showed the activation of all three possible slip plane families, namely {110}, {112} and {123} all owning a ⟨111⟩ Burgers vector at comparable CRSS.

As first crude estimate we want to refer to the stress required to move a dislocation through a lattice, the Peierls stress $\tau_p = \frac{2G}{1-\nu}\exp(-\frac{2\pi}{(1-\nu)}\frac{d}{b})$ with G being the shear modulus, the Poissonś ratio ν, the lattice spacing d and the magnitude of the Burgers vector b. The Peierls stress on higher index planes should be significantly higher and, therefore, it should be more difficult for dislocations to move on those planes. The Peierls equation above was originally deduced based on the Peierls–Nabarro (P–N) model, where a single straight edge dislocation with a planar core structure in a simple cubic structure was considered at 0 K [32,33]. However, the screw dislocations that dominate the deformation of BCC metals are believed to have non-planar structures and move forward through the kink-pair mechanism including nucleation of a kink-pair and lateral motion of the kinks. Temperature and stress have a great influence on the core structure and hence the kink-pair formation [20,34] which renders slip in bcc more complex. Therefore, it is not reasonable to assess the possibility of the activated slip systems merely based on the Peierls stress of the P–N model. The simple Peierls stress approach does not work [32–34].

Our result is complementary to the observations reported in references [35–38] showing the activation of {110} and {112} slip planes only. A possible explanation for the additional activation of {123} slip is that the former studies of Du et al. [35] and Franciosi et al. [38] were not conducted on orientations favoring {123} slip (e.g., see Fig. 8). Although constant efforts have been made to explain the hardening/softening of iron caused by the addition of the foreign atoms, their complex influence on the activation of slip planes still remains an open question [39,40]. Hence, another reason might be that we investigated chemically non-pure iron pillars from a commercial DP800 steel grade and not high purity iron [37].

Let us note that the above mentioned slip planes are all identified by means of SEM images and, therefore, are averaged planes within the resolution provided by field emission SEM microscopy. Caillard concluded from thorough transmission electron microscopy (TEM) investigations with significantly higher lateral resolution that the elementary slip planes are {110} types in Fe, irrespective of the investigated alloying elements (see the work of [19,39–41]). According to Caillard an apparent average plane – as we observed – can be realized by continuous intensive cross slip between two {110} planes. Caillardś view is supported by molecular dynamics simulations from Gilbert et al. [42], who identified that glide on {112} in pure iron is only observed from length scales far above the atomistic one. Also in their case {112} slip occurs via numerous cross-slip events on {110} planes at an atomic scale. Note that the cross slip phenomenon is particularly strong in bcc structures since the plastic deformation is mainly controlled by the slower motion of screw dislocations [43,44]. In light of the atomistic simulations [42] and experimental work [19,39–41] an identical CRSS of slip on {110}, {112}, and {123} can be explained in terms of averaged Schmid factors on constituting, elementary {110} slip planes. It is still interesting to note that the slip traces appear to originate from flat slip planes in the SEM, which requires that the cross-slip process on two elementary {110} planes happens extremely periodically.

A non-Schmid behavior is frequently discussed for bcc [45–47]. In our work, the magnitude of the CRSS of the three slip plane families is within the resolution provided by pillar compression identical for all three systems irrespective of the loading direction. The Schmid factor reasonably well predicts the activation of activated slip systems in ferrite for both steel grades (see Fig. 8). The slip plane experiencing the highest Schmid factor, e.g., the highest resolved shear stress, is in far most cases activated first. This behavior indicates that the non-Schmid phenomena, at least in our case, play a minor role. Nevertheless, occasionally – particularly for the smaller sized pillars and in regions with minor differences in Schmid factors – we observed the activation of the slip plane with the second or third highest Schmid factor. This phenomenon had previously been entitled “Breakdown of Schmidś law” and reflects the important role of the availability and size of dislocation sources

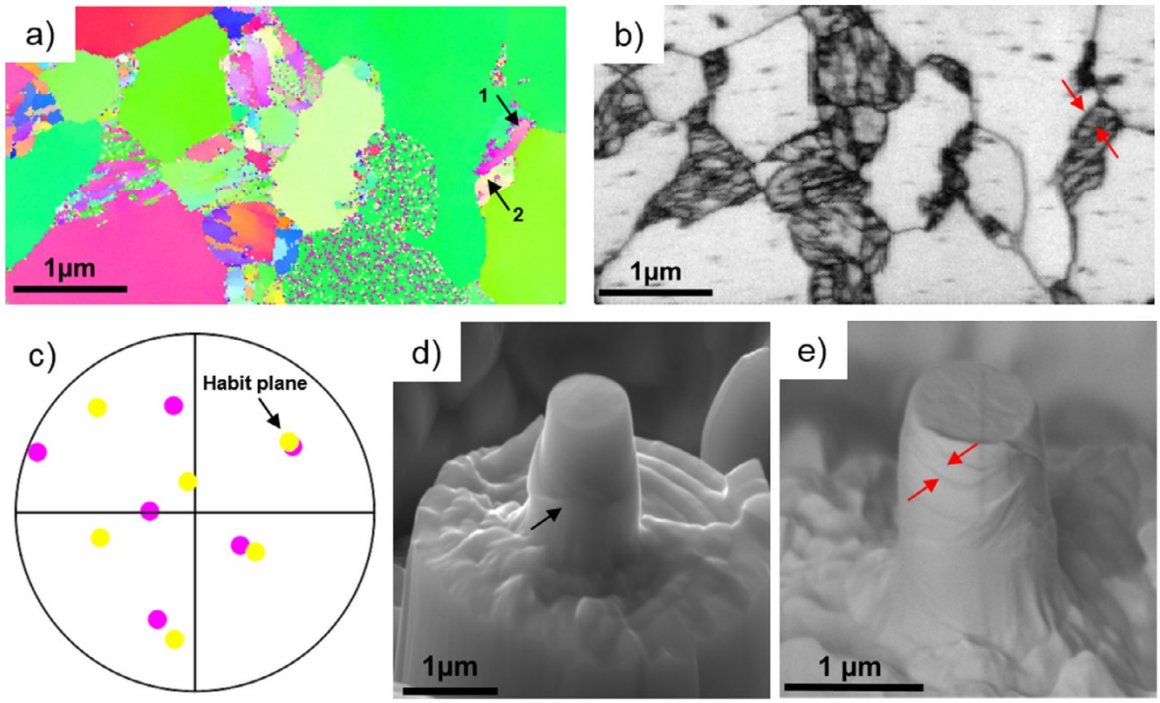

Fig. 10. (a) and (b) IPF and IQ map of DP1 indexed by ferrite to show the substructures of martensite in DP2. (c) Presents the {110} pole figure of substructure 1 and 2 in (a). (d) and (e) show two compressed martensite pillars, where the black arrow indicates sink-in (d) and red arrow the slip trace in (e).

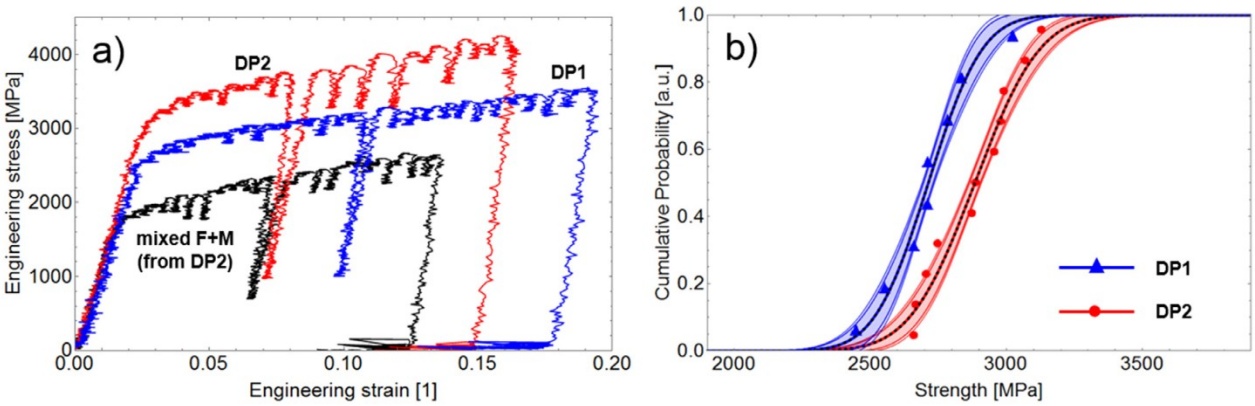

Fig. 11. (a) Engineering stress versus strain curves of martensite micropillars from the two DP800 grades. The black curve represents a martensite pillar which sunk in due to an invisible ferrite base. (b) The distribution of the compressive yield strength extracted at a plastic strain of 0.01 martensite micropillars of DP1 and DP2.

in micron sized samples [26]. Du et al. and Francioso et al. found similar results for {110} and {112} planes [35,38].

4.2. Size effects in DP800 ferrite grains

The breakdown of Schmidś law at small dimensions is not the only consequence of reduced sample dimensions we observe here. Due to the dimensional constraints dislocation sources are potentially smaller in smaller pillars, resulting in a “smaller is stronger” effect [48,49]. This also holds true for both of our DP steels. In our work, smaller pillars indeed exhibit a higher mean CRSS than larger ones (see Table 3). Also, a much larger CRSS dispersion of 2 μm sized pillars exists compared to 3 μm (compare the scatter in Fig. 8b), being another aspect of the size effect (see for instance Bei et al. [50] and Sudharshan Phani et al. [51]).

The dislocation density gradient across the ferrite grain in our dual phase steels as observed via ECCI imaging (see Fig. 2c and d) also contributes to the size scaling in the ferrite grains. A higher dislocation density is observed near the phase boundary between ferrite and martensite to accommodate the volume expansion during the martensitic transformation. This observation is consistent with research work of Tasan et al. [1] and Kadkhodapour et al. [9]. We have milled all our pillars with the intention to locate them in the center of one ferrite grain. Hence, a 3 μm pillar is more likely to contain a higher density of dislocations (therefore dislocation sources) than a 2 μm pillar. Since the number of dislocation sources is known to play a dominant role in the deformation behavior of materials at the micron scale we attribute the significant drop of the CRSS within the small changes of the pillar diameter to the increased number of pre-existing dislocation sources. Hence, the size scaling effect of the CRSS observed here is a sampling effect where larger pillars contain disproportionately more dislocation sources due to the vicinity to the martensite requiring less dislocation source activation stress (see Fig. 8b and c).

4.3. Deformation behavior of martensite

The martensite in both investigated steel grades presents, in accordance with low carbon steel with less than 0.8 wt% C, a lath morphology [52]. The martensite islands in our DP steels exhibit

Table 4
Comparison of the mechanical behavior at the macro and micro scale for both DP steel grades.

	Microscale		Macroscale				Microstructure		
	Ferrite [MPa]	Mart. [MPa]	YS [MPa]	UTS [MPa]	UE [%]	TE [%]	Vol. M [%]	Ferrite G.S. [μm]	Mart. G.S. [μm]
DP1	205 ± 8	2716 ± 62	530	830	8.8	14.4	42 ± 1	5.9 ± 0.1	1.1 ± 0.1
DP2	147 ± 6	2880 ± 49	494	830	11.5	18.6	38 ± 1	7.0 ± 0.1	1.0 ± 0.1

Abbreviations: Vol. M, volume fraction martensite; Mart, martensite; G.S, grain size.

homogenous plasticity with only few deformation traces. The plasticity at the traces is related to the deformation along the block boundaries because the block boundary is {110} plane type that is a potential slip plane family for near bcc martensite. If the block boundary exhibits a high resolved shear stress, gliding along the block boundary is observed [29]. Hence, sliding of block boundaries can enhance plasticity of martensite. However, if the maximum resolved shear stress has a large angle to the block boundary, this interface acts as an effective barrier for dislocation slip and, therefore, restricts plasticity of martensite [31].

In our tests the milled pillars can contain several block boundaries that are even non-parallel to each other if more than one packet exists. As a result, multiple slip systems can be activated. Instead of simple slip traces observed in ferrite, the martensite pillars show barreling in most cases with occasionally local deformation traces along the block boundaries. The local deformation appears to terminate at packet boundaries. These local sliding along the block boundaries might cause the small load drops on the engineering stress versus engineering strain curve, while the packet boundary contributes to the high yield strength of the martensite island. Ghassemi-Armaki et al. [13] found that micropillars containing one packet boundary behave similar to bulk lath martensite in terms of the yield strength. Therefore, we can expect that a bulk martensite comprised of such fine substructures like in our case can reach a yield strength up to 3 GPa.

4.4. Comparison of the DP steel grades

We have studied two dual phase steels and both have identical ultimate strength fitting the DP800 classification. However, under the same tensile test conditions, they show significantly different uniform and fracture elongation as well as yield strength as summarized in Table 4. DP2, with a larger mechanical heterogeneity, unexpectedly exhibits a higher uniform and total elongation that might be caused by a higher work hardening potential of softer ferrite in DP2 and can suppress a rapid growth of cracks. However, the current work does not allow for an quantitative assessment of the local work hardening ability of ferrite and, therefore, additional work at different engineering macro strain levels needs to be done to shine light on the damage behavior.

Besides, we found that ferrite with higher CRSS corresponds to a higher yield strength of dual phase steels which is consistent with the picture of ferrite playing the dominant role in the early yielding behavior. Still, the differences in ferrite CRSS can be discussed. Our APT data shows that the chemical composition of ferrite in both DP steel grades does not vary significantly. Cr is the only element differing, which is entirely in solid solution. The minor chemical variation between the ferrite in the two steel grades cannot explain the strength difference observed in pillar compression.

In contrast to the chemical distribution, the dislocation density is different for both steel grades. The ferrite having a smaller grain size in DP1 possesses a higher dislocation density (see Fig. 2c and d). Hence, we hypothesize without proof that the ferrite CRSS difference at yielding is rather caused by differences of the dislocation density instead of chemistry of ferrite.

By contrast, the carbon distribution and content in martensite of two DPs varies largely. The formation of carbides in DP1 significantly decreases the carbon in the solid solution state (Fig. 4). The C depletion of martensite in DP1 can reduce the strength of martensite by allowing for local dislocation activity. The critical substructure size for deformation in the martensite island is the block width that is approximately 100 nm in both steels (Fig. 2c and d). Hence, we think that the dominating factor for the differences in martensite strength here is the heterogeneous carbon distribution and formation of carbides.

5. Conclusion

We have performed micropillar compression tests on ferrite and martensite in two dual phase steels in order to investigate their micromechanical behavior. Besides investigating and quantifying the microscopic mechanisms of slip in the two phases we also linked the microscopic properties to the macroscopic mechanical behavior in terms of yield strength. Our findings can be summarized as:

- All three slip plane families, namely {110}, {112} and {123} can be activated in ferrite, tested at room temperature and a strain rate of 1×10^{-3}/s. The corresponding CRSS is identical (147 ± 6 MPa, 143 ± 9 MPa and 146 ± 4 MPa) for 3 μm pillars. In the vast majority of the samples the activated slip system can be predicted by the Schmid factor.
- A size effect exists for the single crystalline ferrite pillars. Namely, the CRSS of 2 μm sized pillars is significantly larger than the one of 3 μm pillars (compare 179 ± 11 MPa–147 ± 6 MPa). Besides the current explanations of the sample size effect, the dislocation density gradient from the grain center to the phase boundary plays an important role as the number of pre-existing dislocation sources is disproportionately higher in larger pillars.
- The martensite island yields at a very high strength up to nearly 3 GPa. The pillars mostly exhibit barreling similar to polycrystalline structures under compression. This is caused by the complex substructures and boundaries with a significantly smaller length scale as the pillar diameter. Occasionally, deformation traces occur at block boundaries.
- The two DP steel grades show an identical macroscopic ultimate tensile strength (UTS). However, the individual phases show totally different strength. For instance, the CRSS of ferrite in DP1 and DP2 are 205 ± 8 MPa and 147 ± 6 MPa while the strength of their martensite is 2716 ± 62 MPa and 2880 ± 49 MPa, respectively.
- The ferrite phase is responsible for the early yielding of DP steels. A smaller CRSS of ferrite corresponding to a smaller yield strength of DP steels.

Declaration of Competing Interest

None.

Acknowledgment

Prof. Gerhard Dehm (MPIE) is gratefully acknowledged for his support and discussions. The project was funded by the German research foundation (Deutsche Forschungsgemeinschaft, DFG) within the Collaborative Research Center (TRR 188, “Damage Controlled Forming Processes”, 278868966) in project B03 “Understanding the damage initiation at microstructural scale”.

References

[1] C.C. Tasan, M. Diehl, D. Yan, M. Bechtold, F. Roters, L. Schemmann, C. Zheng, N. Peranio, D. Ponge, M. Koyama, K. Tsuzaki, D. Raabe, An overview of dual-phase steels: advances in microstructure-oriented processing and micromechanically guided design, Annu. Rev. Mater. Res. 45 (1) (2015) 391–431.
[2] M. Calcagnotto, Y. Adachi, D. Ponge, D. Raabe, Deformation and fracture mechanisms in fine- and ultrafine-grained ferrite/martensite dual-phase steels and the effect of aging, Acta Mater. 59 (2) (2011) 658–670.
[3] V.L. de la Concepción, H.N. Lorusso, H.G. Svoboda, Effect of carbon content on microstructure and mechanical properties of dual phase steels, Procedia Mater. Sci. 8 (2015) 1047–1056.
[4] A. Ghatei Kalashami, A. Kermanpur, E. Ghassemali, A. Najafizadeh, Y. Mazaheri, Correlation of microstructure and strain hardening behavior in the ultrafine–grained Nb-bearing dual phase steels, Mater. Sci. Eng. A 678 (2016) 215–226.
[5] Q. Lai, O. Bouaziz, M. Gouné, L. Brassart, M. Verdier, G. Parry, A. Perlade, Y. Bréchet, T. Pardoen, Damage and fracture of dual-phase steels: influence of martensite volume fraction, Mater. Sci. Eng. A 646 (2015) 322–331.
[6] J. Kang, Y. Ososkov, J. Embury, D. Wilkinson, Digital image correlation studies for microscopic strain distribution and damage in dual phase steels, Scr. Mater. 56 (11) (2007) 999–1002.
[7] C.C. Tasan, J.P.M. Hoefnagels, M. Diehl, D. Yan, F. Roters, D. Raabe, Strain localization and damage in dual phase steels investigated by coupled in-situ deformation experiments and crystal plasticity simulations, Int. J. Plast. 63 (2014) 198–210.
[8] C.C. Tasan, M. Diehl, D. Yan, C. Zambaldi, P. Shanthraj, F. Roters, D. Raabe, Integrated experimental–simulation analysis of stress and strain partitioning in multiphase alloys, Acta Mater. 81 (2014) 386–400.
[9] J. Kadkhodapour, S. Schmauder, D. Raabe, S. Ziaei-Rad, U. Weber, M. Calcagnotto, Experimental and numerical study on geometrically necessary dislocations and non-homogeneous mechanical properties of the ferrite phase in dual phase steels, Acta Mater. 59 (11) (2011) 4387–4394.
[10] J. Zhou, A.M. Gokhale, A. Gurumurthy, S.P. Bhat, Realistic microstructural RVE-based simulations of stress–strain behavior of a dual-phase steel having high martensite volume fraction, Mater. Sci. Eng. A 630 (2015) 107–115.
[11] H.J. Bong, H. Lim, M.-.G. Lee, D.T. Fullwood, E.R. Homer, R.H. Wagoner, An RVE procedure for micromechanical prediction of mechanical behavior of dual-phase steel, Mater. Sci. Eng. A 695 (2017) 101–111.
[12] A. Srivastava, H. Ghassemi-Armaki, H. Sung, P. Chen, S. Kumar, A.F. Bower, Micromechanics of plastic deformation and phase transformation in a three-phase TRIP-assisted advanced high strength steel: experiments and modeling, J. Mech. Phys. Solids 78 (2015) 46–69.
[13] H. Ghassemi-Armaki, P. Chen, Shrikant Bhat, Sriram Sadagopan, Sharvan Kumar, Allan Bower, Microscale-calibrated modeling of the deformation response of low-carbon martensite, Acta Mater. 61 (10) (2013) 3640–3652.
[14] H. Ghassemi-Armaki, R. Maaß, S.P. Bhat, S. Sriram, J.R. Greer, K.S. Kumar, Deformation response of ferrite and martensite in a dual-phase steel, Acta Mater. 62 (2014) 197–211.
[15] P. Chen, H. Ghassemi-Armaki, S. Kumar, A. Bower, S. Bhat, S. Sadagopan, Microscale-calibrated modeling of the deformation response of dual-phase steels, Acta Mater. 65 (2014) 133–149.
[16] D.D. Tjahjanto, P. Eisenlohr, F. Roters, Multiscale deep drawing analysis of dual-phase steels using grain cluster-based RGC scheme, Model. Simul. Mater. Sci. Eng. 23 (4) (2015) 17pp, doi:10.1088/0965-0393/23/4/045005.
[17] B. Mohammed, T. Park, F. Pourboghrat, J. Hu, R. Esmaeilpour, F. Abu-Farha, Multiscale crystal plasticity modeling of multiphase advanced high strength steel, Int. J. Solids Struct. 151 (2018) 57–75.
[18] E.-Y. Kim, S.-H. Choi, E.-J. Shin, J. Yoon, Simulation of earing behaviors in bake hardening steel exhibiting a strong off-γ-fiber component, Int. J. Solids Struct. 49 (25) (2012) 3573–3581.
[19] D. Caillard, Kinetics of dislocations in pure Fe. Part I. In situ straining experiments at room temperature, Acta Mater. 58 (9) (2010) 3493–3503.
[20] V. Vitek †, Core structure of screw dislocations in body-centred cubic metals: relation to symmetry and interatomic bonding, Philos. Mag. 84 (3–5) (2004) 415–428.
[21] R. Gröger, V. Vitek, Breakdown of the Schmid law in BCC molybdenum related to the effect of shear stress perpendicular to the slip direction, Mater. Sci. Forum 482 (2005) 123–126.
[22] M.D. Uchic, D.M. Dimiduk, J.N. Florando, W.D. Nix, Sample dimensions influence strength and crystal plasticity, Science 305 (5686) (2004) 986–989.
[23] J.R. Greer, J.T.M. De Hosson, Plasticity in small-sized metallic systems: intrinsic versus extrinsic size effect, Prog. Mater. Sci. 56 (6) (2011) 654–724.
[24] G. Dehm, B.N. Jaya, R. Raghavan, C. Kirchlechner, Overview on micro- and nanomechanical testing: new insights in interface plasticity and fracture at small length scales, Acta Mater. 142 (2018) 248–282.
[25] H. Kitahara, R. Ueji, N. Tsuji, Y. Minamino, Crystallographic features of lath martensite in low-carbon steel, Acta Mater. 54 (5) (2006) 1279–1288.
[26] K.S. Ng, A.H.W. Ngan, Breakdown of Schmid's law in micropillars, Scr. Mater. 59 (7) (2008) 796–799.
[27] J.-Y. Kim, D. Jang, J.R. Greer, Crystallographic orientation and size dependence of tension–compression asymmetry in molybdenum nano-pillars, Int. J. Plast. 28 (1) (2012) 46–52.
[28] J. Senger, D. Weygand, P. Gumbsch, O. Kraft, Discrete dislocation simulations of the plasticity of micro-pillars under uniaxial loading, Scr. Mater. 58 (7) (2008) 587–590.
[29] C. Du, J.P.M. Hoefnagels, R. Vaes, M.G.D. Geers, Plasticity of lath martensite by sliding of substructure boundaries, Scr. Mater. 120 (2016) 37–40.
[30] K. Kwak, T. Mayama, Y. Mine, K. Takashima, Anisotropy of strength and plasticity in lath martensite steel, Mater. Sci. Eng. A 674 (2016) 104–116.
[31] Y. Mine, K. Hirashita, H. Takashima, M. Matsuda, K. Takashima, Micro-tension behaviour of lath martensite structures of carbon steel, Mater. Sci. Eng. A 560 (2013) 535–544.
[32] A. Ngan, A generalized Peierls-Nabarro model for nonplanar screw dislocation cores, J. Mech. Phys. Solids 45 (6) (1997) 903–921.
[33] F.R.N. Nabarro, Fifty-year study of the Peierls-Nabarro stress, Mater. Sci. Eng. A 234-236 (1997) 67–76.
[34] A. Koester, A. Ma, A. Hartmaier, Atomistically informed crystal plasticity model for body-centered cubic iron, Acta Mater. 60 (9) (2012) 3894–3901.
[35] C. Du, F. Maresca, M.G.D. Geers, J.P.M. Hoefnagels, Ferrite slip system activation investigated by uniaxial micro-tensile tests and simulations, Acta Mater. 146 (2018) 314–327.
[36] A.B. Hagen, B.D. Snartland, C. Thaulow, Temperature and orientation effects on the deformation mechanisms of α-Fe micropillars, Acta Mater. 129 (2017) 398–407.
[37] A.B. Hagen, C. Thaulow, Low temperature in-situ micro-compression testing of iron pillars, Mater. Sci. Eng. A 678 (2016) 355–364.
[38] P. Franciosi, L.T. Le, G. Monnet, C. Kahloun, M.H. Chavanne, Investigation of slip system activity in iron at room temperature by SEM and AFM in-situ tensile and compression tests of iron single crystals, Int. J. Plast. 65 (2015) 226–249.
[39] D. Caillard, A TEM in situ study of alloying effects in iron. II—solid solution hardening caused by high concentrations of Si and Cr, Acta Mater. 61 (8) (2013) 2808–2827.
[40] D. Caillard, An in situ study of hardening and softening of iron by carbon interstitials, Acta Mater. 59 (12) (2011) 4974–4989.
[41] D. Caillard, Kinetics of dislocations in pure Fe. Part II. In situ straining experiments at low temperature, Acta Mater. 58 (9) (2010) 3504–3515.
[42] M.R. Gilbert, S. Queyreau, J. Marian, Stress and temperature dependence of screw dislocation mobility inα-Fe by molecular dynamics, Phys. Rev. B 84 (17) (2011).
[43] C.R. Weinberger, B.L. Boyce, C.C. Battaile, Slip planes in bcc transition metals, Int. Mater. Rev. 58 (5) (2013) 296–314.
[44] L. Ventelon, F. Willaime, E. Clouet, D. Rodney, Ab initio investigation of the Peierls potential of screw dislocations in bcc Fe and W, Acta Mater. 61 (11) (2013) 3973–3985.
[45] M. Wen, A.H.W. Ngan, Atomistic simulation of kink-pairs of screw dislocations in body-centred cubic iron, Acta 48 (17) (2000) 4255–4265.
[46] L.M. Hale, J.A. Zimmerman, C.R. Weinberger, Simulations of bcc tantalum screw dislocations: why classical inter-atomic potentials predict {112} slip, Comput. Mater. Sci. 90 (2014) 106–115.
[47] H. Lim, L.M. Hale, J.A. Zimmerman, C.C. Battaile, C.R. Weinberger, A multi-scale model of dislocation plasticity in α-Fe: incorporating temperature, strain rate and non-Schmid effects, Int. J. Plast. 73 (2015) 100–118.
[48] C.A. Volkert, E.T. Lilleodden, Size effects in the deformation of sub-micron Au columns, Philos. Mag. 86 (33–35) (2006) 5567–5579.
[49] D.M. Dimiduk, M.D. Uchic, T.A. Parthasarathy, Size-affected single-slip behavior of pure nickel microcrystals, Acta Mater. 53 (15) (2005) 4065–4077.
[50] H. Bei, S. Shim, G.M. Pharr, E.P. George, Effects of pre-strain on the compressive stress–strain response of Mo-alloy single-crystal micropillars, Acta Mater. 56 (17) (2008) 4762–4770.
[51] P. Sudharshan Phani, K.E. Johanns, G. Duscher, A. Gali, E.P. George, G.M. Pharr, Scanning transmission electron microscope observations of defects in as–grown and pre-strained Mo alloy fibers, Acta Mater. 59 (5) (2011) 2172–2179.
[52] M. Umemoto, E. Yoshitake, I. Tamura, The morphology of martensite in Fe-C, Fe-Ni-C and Fe-Cr-C alloys, J. Mater. Sci. 18 (10) (1983) 2893–2904.